Journal of Materials Chemistry C

ROYAL SOCIETY OF CHEMISTRY

PAPER

View Article Online
View Journal | View Issue

Cite this: J. Mater. Chem. C, 2021, 9, 4971

Auxetic, flexible, and strain-tunable two-dimensional *th*-AlN for photocatalytic visible light water splitting with anisotropic high carrier mobility†

Mehmet Emin Kilic * and Kwang-Ryeol Lee*

Received 30th January 2021,
Accepted 4th March 2021

DOI: 10.1039/d1tc00467k

rsc.li/materials-c

Two-dimensional(2D) materials are considered excellent candidates for achieving a highly efficient photocatalyst. Herein, we report a novel 2D aluminum nitride monolayer (*th*-AlN) as a potential photocatalyst material, possessing robust energetic, dynamical, thermal, and mechanical stability as well as strong stability in aqueous conditions. The monolayer is an indirect band gap semiconductor at its equilibrium state and can induce an indirect-to-direct band gap transition under a very small strain (−4%). The band edge positions fit perfectly the water oxidation and reduction redox potentials. The monolayer exhibits strong visible-ultraviolet light absorption, which is favorable for the efficient utilization of sunlight. The excellent electron transport ability including high and directionally anisotropic carrier mobility (10^4 cm^2 V^{-1} s^{-1}) leads to the rapid separation of electron–hole pairs, retards the recombination of electron–hole pairs, and greatly improves the photocatalytic activity. Furthermore, the monolayer exhibits exceptional mechanical properties including ultrahigh ideal strength (40%) outperforming graphene, good flexibility, and mechanical anisotropy. Remarkably, the negative Poisson's ratio makes *th*-AlN a promising candidate for auxetic materials. With these outstanding properties, *th*-AlN can be considered as a promising candidate for potential application in the fields of electronics, optoelectronics, and nanomechanics.

1 Introduction

Energy harvested directly from sunlight offers a potentially desirable and sustainable approach towards fulfilling future energy demands. Photocatalytic water splitting with solar light is the most promising technology to provide low-cost and clean hydrogen energy.[1,2] The dissociation of water directly into hydrogen and oxygen under sunlight irradiation is the key for photocatalytic hydrogen generation. The development of efficient photocatalysts possessing excellent photocatalytic properties such as an appropriate band gap, band edges straddling the redox potential of water, and efficient visible light absorption capability has been a major challenge. In recent years, hundreds of semiconductors have been investigated for water splitting.[3,4] In particular, 2D semiconductors have attracted much attention for photocatalytic water splitting due to their desirable photocatalytic properties such as large surface area providing the large adsorption capacity of OH, H^+, and H_2O with more active sites, a small charge transport distance, high mobility, and a wide range of electronic properties.[5–7]

Among 2D semiconductors, nitrides have aroused significant research interest as effective photovoltaic materials having unique properties such as low cost, non-toxicity, high stability, and easy synthesis and modification.[8–10] Recently, AlN-based 2D semiconductors have been proposed for photocatalysis.[11–13] From a structural point of view, much attention has been paid to the 2D honeycomb structure of AlN (h-AlN),[14–17] which, however, is not the only possible 2D structure made up of Al and N atoms. We point out that an atom should prefer a spatial arrangement of multiple bonds with its neighbors due to the valence electron pair repulsion rule.[18] The search for new functional 2D materials with unprecedented properties is one among the most intensively researched areas.[19,20]

Recently, significant theoretical efforts have been made to investigate tetra-hexagonal structured 2D materials with superior properties.[21–26] In this work, we predict a novel 2D AlN sheet with a perfectly ordered arrangement of tetragonal (*t*) and

Computational Science Center, Korea Institute of Science and Technology, Seoul 136-791, Republic of Korea. E-mail: mekilic@kist.re.kr, krlee@kist.re.kr

† Electronic supplementary information (ESI) available: Optimized atomic structure and phonon band dispersion of h-AlN; optimized atomic structure, phonon band dispersion, HSE06 functional electronic band structure, and strain–stress relationship of t-AlN; phonon band structure at 10% biaxial strain; AIMD results at 800 K; strain energy with respect to various strains; AIMD results in water at 300 K; variation of bong lengths and bond angles with respect to in-plane axial strains; atom and orbital projected electronic density of states; charge density of VBM and CBM; ELF plot; deformation potential energy with respect to strain for th-AlN. See DOI: 10.1039/d1tc00467k

hexagonal (*h*) rings, named *th*-AlN. To suggest the possibility to fabricate *th*-AlN, we primarily evaluate its stability under ambient conditions in view of dynamical, thermal, and mechanical stabilities by state-of-art theoretical calculations. Next, the stability in the liquid water is expected to be good based on AIMD simulations at T = 300 K. For verifying the good environmental stability of *th*-AlN, we have examined its exceptional properties including, anisotropy, negative Poisson's ratio, ultrahigh ideal strength, decent band gap, desirable band edge positions, high carrier mobility, and strong absorption in the visible region. Finally, we have revealed its potential to be an efficient photocatalyst material for water splitting.

2 Computational methods

Our calculations were carried out using the Vienna *ab-initio* simulation package (VASP),[27] based on density functional theory (DFT). The projector augmented wave (PAW) method[28,29] was used to take into account the electron–ion interactions. A plane-wave basis set with an energy cut-off of 520 eV was employed. The exchange correlation potential was calculated by the generalized gradient approximation (GGA) using the scheme of Perdew, Burke, and Ernzerhof (PBE).[30] The Brillouin zone (BZ) integration was carried out using a 15 × 15 × 1 Γ-centered Monkhorst–Pack (MP) *k*-space sampling grid.[31] The supercells were repeated periodically on the *xy* plane while a vacuum region of about 18 Å was applied along the *z*-direction to avoid the interaction caused by the periodic images. The atomic positions and lattice were fully relaxed until energy and forces were converged to 10^{-5} eV per atom and 0.01 eV Å^{-1}, respectively. To obtain more accurate information on the electronic properties such as band gap and band edge positions, the Heyd–Scuseria–Ernzerhof (HSE06) screened hybrid density functional[32,33] was adopted. The optical properties were studied using GW_0 approximation in conjunction with the Bethe–Salpeter equation (BSE) by taking into account the electron–hole correlations.[34–36] For the GW_0 calculations, a *k*-point set of 8 × 8 × 1 and a cutoff energy of 480 eV were used in order to reduce the computational cost, but the number of bands is increased three times to 144. The lattice dynamics calculations including the phonon frequencies and phonon density of states (PhDOS) were performed using a supercell approach within the Phonopy package[37] where the supercell contains 4 × 4 × 1 unit cells and the corresponding *k*-point sampling uses a 2 × 2 × 1 *k*-mesh grid. To test the thermal stability, the AIMD calculations were performed in the NVT ensemble (by not allowing any change in the volume, V and the total number of atoms, N in the system) using the Nose–Hoover thermostat.[38–40] The total simulation time for the AIMD simulations was taken as 6 ps with a time step of 1 fs.

3 Results and discussion

3.1 Structure characterization

We start to examine the structure characterization of *th*-AlN. The optimized atomic structure is shown in Fig. 1(a). The unit cell, containing 3-fold and 4-fold coordinated atoms (denoted as X^3 and X^4, X = Al, N), belongs to *Pccm* symmetry (space group no 49). The structure consists of three atomic layers where the middle layer is occupied by Al^4 and N^4 atoms while the top and bottom layers are composed of Al^3 and N^3 atoms. For comparison, we initially study the 2D *h*-AlN and *t*-AlN (Fig. S1 and S2, ESI†). The obtained results including the lattice constants, bond length, and phonon spectrum agree well with those previously reported.[9,15,41] Turning our focus to *th*-AlN, the optimized lattice constants are a = 5.473 Å and b = 7.843 Å. The vertical difference between Al^3 atoms in the top and bottom layers is found to be h_1 = 1.096 Å while that between N^3 atoms is h_2 = 1.656 Å. The buckling thickness h = 1.376 Å is the average value of h_1 and h_2. The bond length of Al^3–N^3 about d_1 = 1.726 Å is close to that in *h*-AlN (1.79–1.81 Å[15,17]) and *so*-AlN (1.76–1.83 Å[42]) while the bond lengths of Al^3–N^4 and Al^4-N^3 are d_2 = 1.890 Å and d_3 = 1.906 Å, respectively, which are almost the same as the AlN bond length in *c*-AlN (1.908 Å[43]). Significant electron localization around the Al^3–N^3 bond and electron concentration around N atoms are observed to be the reason for the large electronegativity of N atoms (3.04[44]) with respect to Al atoms (1.6[44]) (Fig. 1(b)).

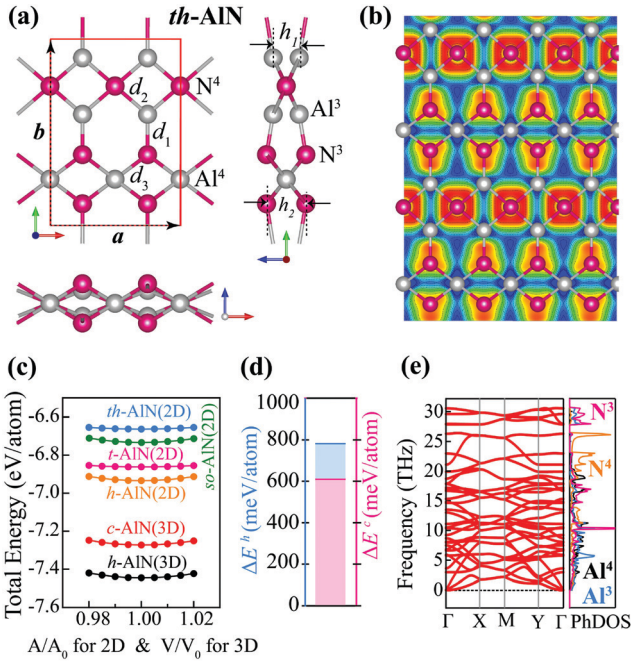

Fig. 1 (a) Top and side views of the *th*-AlN structure with lattice vectors *a* and *b* in the *xy*-plane. The unit cell is framed by a red line inset. (b) Calculated electron localization function (ELF) plot. (c) Total energy per atom with respect to area (volume) of *th*-AlN along with other various 2D (and 3D) allotropes of AlN. (d) The formation energy of *th*-AlN with respect to its cubic zinc blende (*c*-AlN) and hexagonal (*h*-AlN) bulk forms (represented in pink and blue colors, respectively). (e) Calculated phonon band spectrum and phonon density-of-states (PhDOS) of *th*-AlN.

3.2 Stability of free-standing *th*-AlN

To evaluate the possibility of the existence of *th*-AlN, we have tested its energetic, dynamical, thermal, and mechanical stability. The energetic stability is first investigated by comparing the total energy of *th*-AlN with its corresponding 2D counterparts having

the same stoichiometry, such as *h*-AlN, *t*-AlN, and *so*-AlN. The total energy of *th*-AlN (−6.663 eV per atom) is slightly higher than that of so-AlN (−6.737 eV per atom), *t*-AlN (−6.862 eV per atom), and *h*-AlN (−6.934 eV per atom), indicating its relative stability (Fig. 1(c)). The energetic stability is further evaluated by the formation energy difference (ΔE^c and ΔE^h), defined as $\Delta E^c = E_{2D} - {E_{3D}}^c$ and $\Delta E^h = E_{2D} - {E_{3D}}^h$, where E_{2D} is per atom energy of *th*-AlN sheet while ${E_{3D}}^c$ and ${E_{3D}}^h$ are per atom energies of two reference bulk forms, namely cubic zinc blende and hexagonal phases, respectively (Fig. 1(d)). The low energy value of ΔE^c and ΔE^h indicates the easy fabrication of the 2D *th*-AlN material from the corresponding bulk forms. The calculated values of ΔE^c of 610 meV per atom and ΔE^h of 782 meV per atom indicate the possibility of experimental realization of *th*-AlN on the suitable substrate referring to the experimentally synthesized 2D graphydine on the copper surface with ΔE of 823 meV per atom.[45] Considering the low formation energy of ΔE^c = 610 meV per atom, we further examine the possible formation mechanism of *th*-AlN and use 2D *t*-AlN obtained from the cubic zinc blende form. The unit of predicted *th*-AlN is perfectly formed by shifting some atoms in *t*-AlN in the manner shown in Fig. S2 (ESI†).

To further examine the dynamic stability of *th*-AlN, the phonon dispersion curves and PhDOS have been calculated using *ab-initio* lattice dynamics calculations. Referring to Fig. 1(e), *th*-AlN is dynamically stable since the frequency of all phonon modes is positive throughout the BZ. In addition to the strain-free conditions, we further investigate its dynamical stability under strain conditions, which would be useful to take into account the existence of the substrate-induced strain environment. It is clear that *th*-AlN remains robust even under strain (Fig. S3, ESI†).

To further understand the stability of *th*-AlN under ambient conditions, a 4 × 3 supercell has been build to perform the AIMD simulations at a high temperature (∼800 K) for 6 ps. To ensure the thermal equilibrium and detect any bond breaking or bond forming under heat, the potential energy of the system is monitored during the simulation time, and found to be almost constant with fluctuations (Fig. S4, ESI†). A snapshot of the atomic configuration of *th*-AlN for 6 ps is given in the inset of the figure, where we do not detect any bond breaking and structure reformation. Therefore, even at high temperatures, the structure of *th*-AlN remains in its original configuration. Despite the short simulation time of 6 ps (which is long enough for the AIMD simulations), we were able to verify that *th*-AlN is thermally stable with respect to the thermal shock.

Finally, we have tested the mechanical stability of *th*-AlN using the following Born–Huang elastic stability criteria:[46] ${C_{11}C_{22}}-{C_{12}}^2 > 0$ and $C_{66} > 0$ where C_{11}, C_{22}, C_{12}, and C_{66} are the elastic stiffness constants obtained by fitting the curve of the energy-strain relationship (Fig. S5, ESI†). The obtained C_{11}, C_{22}, C_{12}, and C_{66} values are respectively 119.23 N m^{-1}, 90.80 N m^{-1}, −4.66 N m^{-1}, and 10.82 N m^{-1}, obeying the Born–Huang criteria for *th*-AlN, and thus, confirms its mechanical stability. All these suggest that the fabrication and application of *th*-AlN are highly possible in experiments.

3.3 Stability of *th*-AlN in water

After verifying the stability of free-standing *th*-AlN, we have investigated its stability in liquid water, which is essential for photocatalyst applications. The AIMD simulations were performed to evaluate its stability in aqueous conditions. As shown in Fig. S6, ESI,† according to the variation of potential energy, the atoms of *th*-AlN in the water only vibrate around their lattice at T = 300 K for 6 ps. Moreover, the snapshot structure at the end of the simulation time shows that *th*-AlN possesses strong stability in the water solution, suggesting that it has the potential to be an efficient photocatalyst where the material should be insoluble in water.

3.4 Mechanical properties

Following the investigation on the stability of *th*-AlN, we then examine the intrinsic mechanical properties including Young's modulus, Poisson's ratio, and ideal strength. The anisotropic

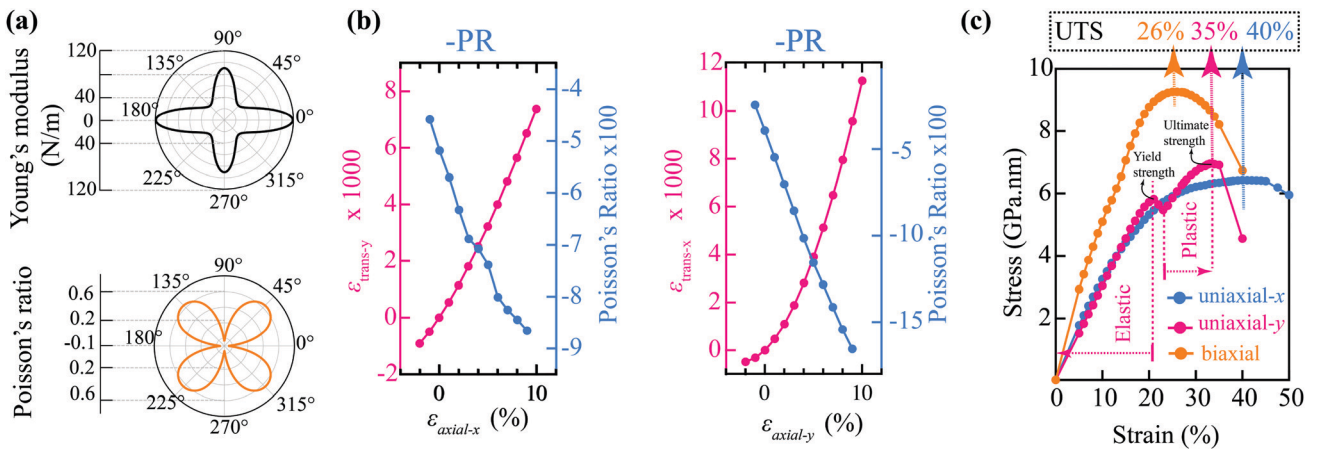

Fig. 2 (a) Calculated orientation-dependent Young's modulus and Poisson's ratio of *th*-AlN. (b) Variation of transverse strain (depicted by pink) and Poisson's ratio (depicted by sky blue) with respect to axial strain ranging from −4% to 10% in the *x* and *y*-directions. (c) Stress–strain relationship for uniaxial strain in the *x* and *y* directions (denoted as uniaxial-*x* and uniaxial-*y*, respectively) and equi-biaxial strain where the ultimate tensile strength (UTS) values are depicted by dashed arrows.

structure of *th*-AlN could yield anisotropic mechanical properties. To explore the directionality further, we have calculated the angular dependence of Young's modulus $Y^{2D}(\theta)$ and Poisson's ratio $\nu(\theta)$. Fig. 2(a) obviously shows that both are highly direction dependent, and indicates anisotropy well. The calculated Y^{2D} along the [100], [010], and [110] (or 0°, 90°, and 45°) directions is about 119.05 N m^{-1}, 90.56 N m^{-1}, and ~35 N m^{-1}, respectively, which are relatively lower than that of *h*-AlN (116 N m^{-1})[41] and MoS_2 (128 N m^{-1}).[47] Compared with other 2D materials such as graphene (340 N m^{-1}),[48] *h*-BN (292.1 N m^{-1}),[49] and tetrahexacarbon (287 N m^{-1}),[23] *th*-AlN possesses much more smaller Young's modulus. The low Young's modulus with directionality makes *th*-AlN promising for next-generation flexible mechanical electronic device applications.

Next, we have calculated the Poisson's ratio (PR), which is the ratio between transverse strain (ε_{trans}) and applied axial strain (ε_{axial}) along the stretch direction and is defined as $\nu = -\varepsilon_{trans}/\varepsilon_{axial}$. The PR of *th*-AlN is found to be $\nu_{xy} = -0.04$ and $\nu_{yx} = -0.05$, where ν_{xy} refers to the axial strain in the *x* direction and transverse strain in the *y* direction. The negative value of PR makes *th*-AlN an "auxetic" material, which is unusual for group-III nitrides and emphasizes its wide range of potential applications. In order to enhance the intrinsic auxetic effect in *th*-AlN, we further examined the PR by strain engineering. Using the finite difference method,[50,51] we have calculated the PR within the large axial strain ranging from −4% to 10% to depict the nonlinear lattice response for finite strain. The variation of response strain and PR to the corresponding axial strain is presented in Fig. 2(b), where ν_{xy} and ν_{yx} are always negative and increases with increasing strain. Thus, the large strain improves the auxetic effect in *th*-AlN. To understand the mechanism of the auxetic effect, we have analyzed the variation of the bond lengths, thickness, bond angles, and dihedral angles of *th*-AlN with respect to the corresponding strain, *e.g.*, when the structure was subjected to uniaxial strain in the *x*-direction, all the bond lengths along the *y*-direction were elongated (Fig. S7, ESI†). The increase in the corresponding bond lengths, the decrease in the thickness, and the nearly constant dihedral angle of Φ_{1234} with an increase in the axial strain, combined together, act as the primary factor of the response strain.

The ideal strength[52] as an extremely important inherent mechanical property shows the upper limit of the strength at which the lattice becomes mechanically unstable. A 2 × 2 supercell has been build to evaluate the ideal strength (or ultimate tensile strength, UTS) of *th*-AlN by applying axial tensile deformations. The variation of stress with axial strain in the *x* and *y* directions and equi-biaxial strain is illustrated in Fig. 2(c). The UTS of *th*-AlN is found to be 40%, 35%, and 26% for uniaxial-*x*, uniaxial-*y*, and equi-biaxial strains, respectively, which is higher when compared to that of other 2D materials such as graphene, *e.g.*, the UTS of pristine graphene, pentagraphene, tetrahexcarbon, and hexagonal boron nitride was reported as ~27%,[53] 21%,[54] 20%,[23] and 30%,[55] respectively, which are lower than that of *th*-AlN. To the best of our knowledge, the UTS of 40% is the highest value for 2D materials. In addition to the flexibility and auxetic behavior with anisotropy, the ultrahigh ideal strength makes *th*-AlN a versatile material for many promising applications.

3.5 Electronic and photocatalytic properties for water splitting

To examine the electronic properties of *th*-AlN, we have calculated the electronic band structure. Fig. 3(a) shows that *th*-AlN is a natural semiconductor with a band gap of 2.59 eV using the HSE06 functional. The obtained electronic band gap of *th*-AlN is much lower than that of the experimentally realized 2D AlN (~9.6 eV).[56,57] The conduction band minimum (CBM) of *th*-AlN is located at the Γ point of the 2D BZ while its valence band maximum (VBM) is settled between the Γ and *X* points (slightly offset from the *X* point), revealing an indirect band gap feature. Its direct band gap at the Γ point is only slightly lower in energy (2.47 eV), which is achieved by strain engineering with −4% strain. On analyzing the partial density of states (pDOS), it is observed that the VBM and CBM are mainly

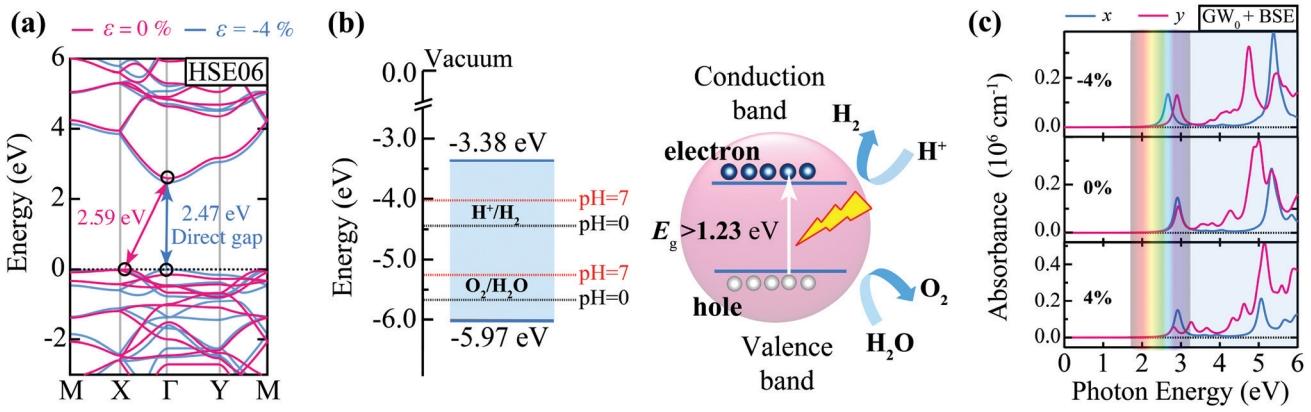

Fig. 3 (a) Electronic band structure for strain-free and strained (−4% equi-biaxial compression) *th*-AlN, depicted as pink and sky blue lines, respectively. (b) (Left) band edge positions (VBM and CBM) of *th*-AlN with respect to vacuum level and (right) schematic of water splitting using the semiconductor photocatalyst. (c) Variation of optical absorbance coefficient with respect to equi-biaxial strain computed using GW_0 + BSE approximation. Absorption coefficients along the *x* and *y* directions are depicted as sky blue and pink, respectively. The color spectrum represents a visible light energy range.

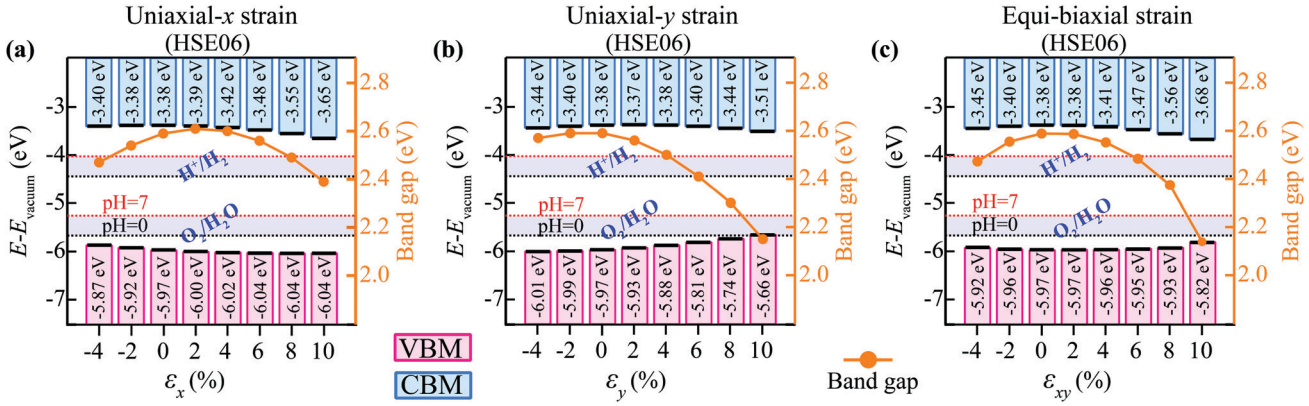

Fig. 4 The variation of the band edge position of the VBM (depicted as pink bars) and CBM (depicted as sky blue bars) and band gap energy (depicted as orange points with orange line) computed using the HSE06 functional of *th*-AlN with respect to (a) uniaxial-*x* (b) uniaxial-*y*, and equi-biaxial strains. The black dashed and red dashed lines represent the redox potential of water splitting at pH = 0 and pH = 7, respectively.

contributed by the p orbitals of N^3 atoms in *th*-AlN (Fig. S8, ESI†), which is also confirmed by the charge distribution of the band edges and the patterns of the electron localization function (ELF) (Fig. S9 and S10, ESI†).

Considering the fundamental requirements for water splitting including good stability, suitable band gap, and appropriate band edge positions, *th*-AlN is evaluated as an efficient photocatalyst for water splitting as the band gap of *th*-AlN of about 2.47 eV is larger than the minimum energy required for the water splitting reaction (1.23 eV). In addition to the band gap requirement, the band edge positions of *th*-AlN perfectly stride the redox potential of water. The energy level of the CBM of about −3.38 eV is much higher than the reduction potential of H^+/H_2 (E_{H^+/H_2} = −4.44 eV + pH × 0.059 eV). The energy level of the VBM of about −5.97 eV is much lower than the oxidation potential of O_2/H_2O (E_{O_2/H_2O} = −5.67 eV + pH × 0.059 eV), as depicted in Fig. 3(b). Remarkably, the corresponding band edge positions fit perfectly the water oxidation and reduction potential in both an acidic environment (pH = 0) and a neutral environment (pH = 7).

Besides the suitable band gap and appropriate band alignment of *th*-AlN, the optical absorption capability in the range of solar cells is also significant for the photocatalytic efficiency. It is then interesting to examine the optical absorption spectrum of *th*-AlN using the state-of-the-art GW_0 + BSE approach. We have calculated the absorption coefficient with polarization vectors parallel to the layer plane. Fig. 3(c) shows that the prominent absorption peaks are located at ∼2.4 eV in the visible range. The spectral absorption in the blue and UV range is even stronger. Hence, *th*-AlN absorbs significant light within the visible-UV region (more than 45% of solar energy[58]). The high photon-harvesting ability in the visible sunlight region and high carrier mobility enable it to act as an efficient photocatalyst for water splitting. As a consequence, the most significant criteria for water splitting are clearly met by *th*-AlN.

3.6 Indirect-to-direct band gap transition and band edge tuning *via* strain engineering

Achieving a direct band gap in *th*-AlN is highly desirable as the indirect band gap feature may assist potential applications in electronic and optoelectronic devices. This obstacle can be overcome by strain engineering. Remarkably, we have realized that *th*-AlN at −4% equi-biaxial strain undergoes an indirect-to-direct band gap transition with 2.47 eV band gap energy (calculated by the HSE06 functional) where the VBM and CBM are located at the Γ point (Fig. 3(a)). Besides the HSE06 calculations, the GW_0 calculations, taking the electron–hole effect into account, also confirm that *th*-AlN subjected to −4% biaxial strain is a direct-gap semiconductor having a GW_0 electronic band gap of 3.52 eV with the VBM and CBM at the Γ point. The optical absorption peak of the strained *th*-AlN along the *x* and *y* directions has different absorption energies. The first absorption peaks for the strained *th*-AlN are located at 2.54 eV and 2.72 eV along the *x* and *y* directions, respectively (Fig. 3(c)). The *th*-AlN exhibits strong anisotropic properties due to the inherent anisotropy (*i.e.* 3-fold coordinated Al and N atoms only lie on the *y*-axis.), which may induce different absorption peaks under strain conditions. Moreover, we analyzed the band edge positions and band gap energy with respect to

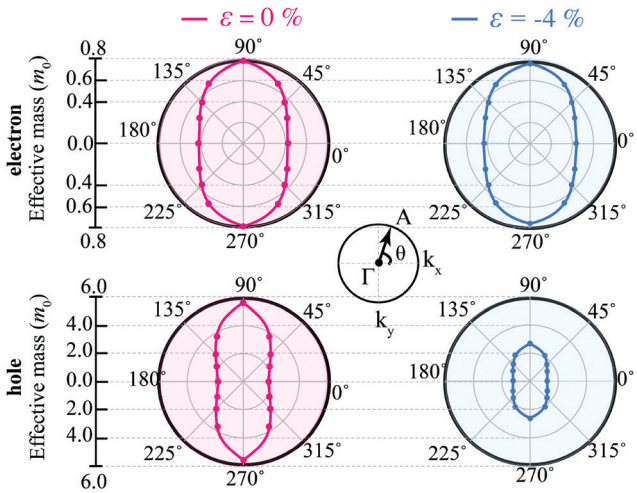

Fig. 5 Angular dependent effective mass of electrons and holes from the Γ–X direction to an arbitrary Γ–A direction for strain-free and strained (−4% equi-biaxial strain) *th*-AlN.

Table 1 Carrier effective mass m^* (m_0 is the mass of free electrons) along Γ–X and Γ–Y directions, in-plane elastic constants C in N m^{-1}, deformation potential E' in eV, and carrier mobility μ in (cm^2 V^{-1} s^{-1}) of *th*-AlN along the x and y directions at room temperature T = 300 K

	m_x^*/m_0	m_y^*/m_0	C_x	C_y	E_x'	E_y'	μ_x	μ_y
Electron	0.43	0.79	119.23	90.80	0.83	0.32	1.48×10^4	4.14×10^4
Hole	1.78	5.60	119.23	90.80	1.90	1.95	0.13×10^4	0.03×10^4

strain (uniaxial and equi-biaxial) in the range from −4% to +10%, as both determine the functionality of *th*-AlN in many optoelectronic applications such as photovoltaics and photoelectrochemical cells. We have observed that *th*-AlN is very sensitive to external strain. Fig. 4 clearly shows that the band gap energy and band edge positions can be tunable by strain engineering. For instance, the band gap energy decreases with increasing compressive and tensile strain. More fascinatingly, the band gap and band edge positions of *th*-AlN are an excellent match with the water splitting energy levels even when subjected to uniaxial and biaxial strains (compressive and tensile). Thus, the strain-imposed *th*-AlN is also quite exciting for solar water splitting.

3.7 Small effective mass and high carrier mobility

A long carrier lifetime and high carrier mobility make the material a promising candidate for optoelectronic devices. More specifically, the rapid separation and slow recombination of photo-generated electrons and holes and extending the life time of charge carriers are crucial for efficient photocatalytic activity. To assess the electron–hole recombination and separation, we investigate the effective mass (m^*) and carrier transport (μ) of *th*-AlN. The effective mass of carriers can be obtained by quadratic fitting of energies E near band edges (VBM/CBM) as: $m^* = \hbar^2(d^2E(k)/dk^2)^{-1}$ where $\hbar$ and k are the reduced Planck constant and wave vector, respectively. The results of the angular dependent effective mass of the electron (m_x^*) and hole (m_h^*) are shown in Fig. 5 and are given in Table 1. The hole effective mass along the Γ–X and Γ–Y directions is found to be $1.78m_0$ and $5.60m_0$ while the electron effective mass is about $0.43m_0$ and $0.79m_0$, respectively. The large difference between m_e^* and m_h^* indicates that the photo-generated electron–hole pairs would move separately with a lower recombination rate.

To further examine the carrier mobility of *th*-AlN, we obtain the deformation potential (E_i') by computing the total energy change of the VBM and CBM with respect to the vacuum level as a function of the axial strain (ε) along the transport direction i (Fig. S11, ESI†). Based on the obtained m_i^*, elastic constant C_i, and E_i', we calculate the room temperature carrier mobility along the transport direction i (x and y) using the following expression: $\mu_i = \dfrac{e\hbar^3 C_i}{(2\pi)^3 k_{1'B} T m_i^* m_d E_i'^2}$ where $m_d = \sqrt{m_x^* m_y^*}$ is the density-of-state mass. As listed in Table 1, *th*-AlN exhibits high electron and hole mobilities along the x and y directions, *i.e.*, $\mu_x^{e} = 1.48 \times 10^4$ cm^2 V^{-1} s^{-1}, $\mu_y^{e} = 4.14 \times 10^4$ cm^2 V^{-1} s^{-1}, $\mu_x^{h} = 0.13 \times 10^4$ cm^2 V^{-1} s^{-1} and $\mu_y^{h} = 0.03 \times 10^4$ cm^2 V^{-1} s^{-1}. Thus, the high carrier mobilities with distinct anisotropy are able to decrease the recombination rate of photogenerated electrons and holes and thus enhance the photocatalytic water splitting efficiency.

4 Conclusions

In conclusion, we have predicted a new 2D aluminum nitride monolayer. Our first-principles calculations have revealed its stability based on energetic, dynamical, thermal, and mechanical aspects and also showed its structural stability in water. *th*-AlN is a semiconductor, having an indirect band gap of 2.59 eV. We have revealed that the band gap can be modulated by strain engineering. The indirect-to-direct band gap transition occurs at −4% biaxial strain. The position of band edges perfectly matches with the water redox potentials. The monolayer exhibits strong visible–ultraviolet light absorption, and high and directionally anisotropic carrier mobility (10^4 cm^2 V^{-1} s^{-1}). Considering the 2D structure with large specific surface area, non-toxicity, suitable band gap, appropriate band edge positions, good optical absorption, high carrier mobility, and anisotropy, *th*-AlN is a promising candidate for efficient photocatalytic water splitting. Furthermore, we have revealed that *th*-AlN is an auxetic semiconductor, possessing a negative Poisson's ratio, and exhibits exceptional mechanical properties such as ultrahigh ideal strength (40%) outperforming graphene, good flexibility, and mechanical anisotropy. Hence, all these outstanding results indicate the wide applicability of *th*-AlN in the fields of optoelectronics, nanoelectronics, and nanomechanics.

Conflicts of interest

There are no conflicts to declare.

Acknowledgements

This work was supported by the Brain Pool Program through the National Research Foundation of Korea (NRF) funded by the Ministry of Science and ICT (2020H1D3A1A02081517) and the Nano Materials Research Program through the Ministry of Science and IT Technology under project No. NRF-2016M3A7B4025402.

References

1 A. Fujishima and K. Honda, *Nature*, 1972, **238**, 37–38.
2 R. M. Navarro Yerga, M. C. Álvarez Galván, F. Del Valle, J. A. Villoria de la Mano and J. L. Fierro, *ChemSusChem*, 2009, **2**, 471–485.
3 K. Maeda and K. Domen, *J. Phys. Chem. Lett.*, 2010, **1**, 2655–2661.

4 T. Hisatomi, J. Kubota and K. Domen, *Chem. Soc. Rev.*, 2014, **43**, 7520–7535.
5 A. K. Singh, K. Mathew, H. L. Zhuang and R. G. Hennig, *J. Phys. Chem. Lett.*, 2015, **6**, 1087–1098.
6 Y. Li, Y.-L. Li, B. Sa and R. Ahuja, *Catal. Sci. Technol.*, 2017, **7**, 545–559.
7 P. Ganguly, M. Harb, Z. Cao, L. Cavallo, A. Breen, S. Dervin, D. D. Dionysiou and S. C. Pillai, *ACS Energy Lett.*, 2019, **4**, 1687–1709.
8 X. Wang, K. Maeda, A. Thomas, K. Takanabe, G. Xin, J. M. Carlsson, K. Domen and M. Antonietti, *Nat. Mater.*, 2009, **8**, 76–80.
9 H. L. Zhuang, A. K. Singh and R. G. Hennig, *Phys. Rev. B: Condens. Matter Mater. Phys.*, 2013, **87**, 165415.
10 L. Lin, Z. Yu and X. Wang, *Angew. Chem.*, 2019, **131**, 6225–6236.
11 P. Liu, A. De Sarkar and R. Ahuja, *Comput. Mater. Sci.*, 2014, **86**, 206–210.
12 Q. Yang, C.-J. Tan, R.-S. Meng, J.-K. Jiang, Q.-H. Liang, X. Sun, D.-G. Yang and X.-P. Chen, *IEEE Electron Device Lett.*, 2016, **38**, 145–148.
13 G. Wang, S. Dang, P. Zhang, S. Xiao, C. Wang and M. Zhong, *J. Phys. D: Appl. Phys.*, 2017, **51**, 025109.
14 P. Tsipas, S. Kassavetis, D. Tsoutsou, E. Xenogiannopoulou, E. Golias, S. Giamini, C. Grazianetti, D. Chiappe, A. Molle and M. Fanciulli, *Appl. Phys. Lett.*, 2013, **103**, 251605.
15 C. Bacaksiz, H. Sahin, H. Ozaydin, S. Horzum, R. T. Senger and F. M. Peeters, *Phys. Rev. B: Condens. Matter Mater. Phys.*, 2015, **91**, 085430.
16 F. Yang, L. Jin, L. Sun, X. Ren, X. Duan, H. Cheng, Y. Xu, X. Zhang, Z. Lai and W. Chen, *Adv. Mater.*, 2018, **30**, 1801891.
17 A. Sengupta, *Appl. Surf. Sci.*, 2018, **451**, 141–147.
18 E. Billo, *Modern inorganic chemistry*, jolly, william l., 1985.
19 R. Pekoz, M. Konuk, M. E. Kilic and E. Durgun, *ACS Omega*, 2018, **3**, 1815–1822.
20 S. Ipek, M. Kilic, A. Mogulkoc, S. Cahangirov and E. Durgun, *Phys. Rev. B*, 2018, **98**, 241408.
21 B. Ram and H. Mizuseki, *Carbon*, 2018, **137**, 266–273.
22 F. M. de Vasconcelos, A. G. Souza Filho, V. Meunier and E. C. Girão, *Phys. Rev. Mater.*, 2019, **3**, 066002.
23 M. E. Kilic and K.-R. Lee, *Carbon*, 2020, **161**, 71.
24 M. E. Kilic and K.-R. Lee, *J. Phys. Chem. C*, 2020, **124**, 8225.
25 F. M. De Vasconcelos, A. G. Souza Filho, V. Meunier and E. C. Girão, *Carbon*, 2020, **167**, 403–413.
26 M. E. Kilic and K.-R. Lee, *Carbon*, 2021, **174**, 368–381.
27 G. Kresse and J. Hafner, *J. Phys.: Condens. Matter*, 1994, **6**, 8245.
28 P. E. Blöchl, *Phys. Rev. B: Condens. Matter Mater. Phys.*, 1994, **50**, 17953.
29 G. Kresse and D. Joubert, *Phys. Rev. B: Condens. Matter Mater. Phys.*, 1999, **59**, 1758.
30 J. P. Perdew, K. Burke and M. Ernzerhof, *Phys. Rev. Lett.*, 1996, **77**, 3865.
31 H. J. Monkhorst and J. D. Pack, *Phys. Rev. B: Solid State*, 1976, **13**, 5188.
32 J. Heyd, G. E. Scuseria and M. Ernzerhof, *J. Chem. Phys.*, 2003, **118**, 8207–8215.
33 J. Paier, M. Marsman, K. Hummer, G. Kresse, I. C. Gerber and J. G. Ángyán, *J. Chem. Phys.*, 2006, **124**, 154709.
34 G. Onida, L. Reining and A. Rubio, *Rev. Mod. Phys.*, 2002, **74**, 601.
35 S. Albrecht, L. Reining, R. Del Sole and G. Onida, *Phys. Rev. Lett.*, 1998, **80**, 4510.
36 M. Rohlfing and S. G. Louie, *Phys. Rev. Lett.*, 1998, **81**, 2312.
37 L. Chaput, A. Togo, I. Tanaka and G. Hug, *Phys. Rev. B: Condens. Matter Mater. Phys.*, 2011, **84**, 094302.
38 S. Nosé, *J. Chem. Phys.*, 1984, **81**, 511–519.
39 S. Nosé, *Mol. Phys.*, 1984, **52**, 255–268.
40 W. G. Hoover, *Phys. Rev. A: At., Mol., Opt. Phys.*, 1985, **31**, 1695.
41 H. Sahin, S. Cahangirov, M. Topsakal, E. Bekaroglu, E. Akturk, R. T. Senger and S. Ciraci, *Phys. Rev. B: Condens. Matter Mater. Phys.*, 2009, **80**, 155453.
42 E. Gürbüz, S. Cahangirov, E. Durgun and S. Ciraci, *Phys. Rev. B*, 2017, **96**, 205427.
43 L.-J. Shi and B.-G. Liu, *Phys. Rev. B: Condens. Matter Mater. Phys.*, 2007, **76**, 115201.
44 A. L. Allred, *J. Inorg. Nucl. Chem.*, 1961, **17**, 215–221.
45 G. Li, Y. Li, H. Liu, Y. Guo, Y. Li and D. Zhu, *Chem. Commun.*, 2010, **46**, 3256–3258.
46 M. Born and K. Huang, *Dynamical Theory of Crystal Lattices*, Oxford, 1954.
47 Y. Cai, G. Zhang and Y.-W. Zhang, *J. Am. Chem. Soc.*, 2014, **136**, 6269–6275.
48 C. Lee, X. Wei, J. W. Kysar and J. Hone, *Science*, 2008, **321**, 385–388.
49 L. Song, L. Ci, H. Lu, P. B. Sorokin, C. Jin, J. Ni, A. G. Kvashnin, D. G. Kvashnin, J. Lou and B. I. Yakobson, *Nano Lett.*, 2010, **10**, 3209–3215.
50 D. T. Ho, S.-D. Park, S.-Y. Kwon, K. Park and S. Y. Kim, *Nat. Commun.*, 2014, **5**, 1–8.
51 J.-W. Jiang and H. S. Park, *Nano Lett.*, 2016, **16**, 2657–2662.
52 T. Li, J. Morris Jr, N. Nagasako, S. Kuramoto and D. Chrzan, *Phys. Rev. Lett.*, 2007, **98**, 105503.
53 F. Liu, P. Ming and J. Li, *Phys. Rev. B: Condens. Matter Mater. Phys.*, 2007, **76**, 064120.
54 S. Zhang, J. Zhou, Q. Wang, X. Chen, Y. Kawazoe and P. Jena, *Proc. Natl. Acad. Sci. U. S. A.*, 2015, **112**, 2372–2377.
55 Q. Peng, W. Ji and S. De, *Comput. Mater. Sci.*, 2012, **56**, 11–17.
56 P. Wang, T. Wang, H. Wang, X. Sun, P. Huang, B. Sheng, X. Rong, X. Zheng, Z. Chen and Y. Wang, *et al.*, *Adv. Funct. Mater.*, 2019, **29**, 1902608.
57 W. Wang, Y. Zheng, X. Li, Y. Li, H. Zhao, L. Huang, Z. Yang, X. Zhang and G. Li, *Adv. Mater.*, 2019, **31**, 1803448.
58 M. Ni, M. K. Leung, D. Y. Leung and K. Sumathy, *Renewable Sustainable Energy Rev.*, 2007, **11**, 401–425.